Chapter VI

Schiff Base Driven Denticity-Fluctuated Structural Assortment of Zinc-pseudohalide Complexes: Synthesis, Structures and Electrical Transport Properties

6.1. Introduction

The newly designed metal incorporated crystalline materials have been considered an emerging field of research as new structures with promising properties of the solids may divulge important avenues in science and technology.[1-4] The development of new metal-based crystalline materials was significant for extrapolating new physicochemical properties and functionalities, leading to the improvement of intelligent molecular devices and applications.[5-15] In the present context of scientific development, coordination driven materials have emerged as a wealth of advanced functional materials such as novel molecular magnets[5-8], smart optics and electronics[9], emerging catalysts[10-13], alloys and composites[14,15], and others[16-19].

Nowadays, design and innovations in molecular electronics was an intensive area of scientific and applied research.[2-22] The foremost applications of molecular electronics include developing innovative materials, logic and memory devices, molecular-scale transistors and energy transduction devices sensors, molecular motors etc.[5-27] In general, molecular electronics may be envisioned as futuristic device miniaturization. The importance of the materials in the development of smart electronic devices stems from their intrinsic electronic properties and the nature of electrolytes, the orientation of molecules, non-covalent interactions, self-assembled structures, and others.[28-32] Therefore, understanding, modelling, controlling, and stimulating the electron conductive properties of the newly designed materials is the crucial need of the hour.

Recently, transition metal-Schiff base complexes are of great interest towards research community because of their outstanding optical power limiting performance, electroluminescence properties and charge transport properties.[33] Work on estimation of electron and hole injections of a monolayer LED devices has explored the new dimension of electrical transport phenomena of Schiff base complexes. Generally, tailor-made zinc complexes containing Schiff base ligands present an embryonic class of energy harvesting materials owing to their cost-effectiveness, thermal stability, color tunability, efficient and intense emission properties, fine-tuning band gap energy,

diversified molecular frameworks etc.[34-37] Further, zinc(II)-Schiff base complexes facilitates the decrement of the energy values for electron and hole reorganization boosting the hole intrinsic mobility to a larger extent which helps the zinc-Schiff base compounds as the potential candidates for designing electrical charge transport applications.[38, 39]

The elucidation of the role of different components like the nature of metal ions, packing of molecules, presence of non-covalent interactions was significant to tune the charge transport properties in molecular electronics. Herein, I report the interesting chelation behaviour of a polydentate Schiff base in forming zinc complexes in presence of pseudohalides. The structural characteristics have been done with different spectroscopic and analytical methods. Single crystal X-ray structural analysis suggested that the Schiff base adopts a zwitterionic form to bind with the zinc ion as a monodentate/bidentate ligand in the presence of thiocyanate ions and lead to mononuclear zinc(II)-Schiff base complex **5**. In contrast, under an identical reaction condition, the same Schiff base behaves as a tridentate chelator in the presence of azide ion leading to a dinuclear zinc-Schiff base-azide complex **6**. Crystal engineering approach, Hirshfeld surface and energy framework analysis of the complexes delineate the dominant contribution of H···S/N hydrogen bonding and C—H···π interactions for a structural assortment of the compounds. A study on AC conductivity under the dark chamber and in the presence of a shower of photon on the zinc complexes were carried out to explore the enhancement of AC conductivity and change in relaxation times of the constructed devices. The electrical conductivity of the zinc complexes as devices A and B in solid state can be explained with a crystal engineering approach and energy framework analysis.

6.2. Experimental Section

6.2.1. Preparation of the complex

6.2.1.1. Materials and Methods

Highly pure *o*-vanillin (Sigma Aldrich, USA), *o*-anisidine (Sigma Aldrich, USA), zinc(II) perchlorate hexahydrate (Merck, India) and sodium azide, ammonium thiocyanate were purchased from the respective concerns. All other chemicals and solvents were of analytical grade and were used as received without further purification.

Caution! Perchlorate salts of metal ions were potentially explosive, especially in organic ligands. Only a small amount of material should be prepared, and it should be handled with care.

6.2.1.2. Synthesis of the Schiff base L^4, zinc complexes 5 and 6

The synthetic procedure of the previously reported chapter V Schiff base ligand, **L^4** was described elsewhere.[40,41] The Schiff base ligand was synthesized by refluxing *o*-anisidine (0.123 g, 1 mmol) with *o*-vanilin (0.152 g, 1 mmol) in 20 ml ethanol for 6 h. The reddish coloured crystalline product was extracted upon evaporating the solution on a water bath. The compound was stored *in vaccuo* over $CaCl_2$ for subsequent use.

A methanolic solution of hydrated $Zn(ClO_4)_2$ (0.370 g, 1 mmol) was added dropwise to the methanol solution of **L^4** (0.270 g, 2 mmol). Afterwards, solid NH_4SCN (0.152 g, 2 mmol) / solid NaN_3 (0.130 g, 2 mmol) was mixed with the reaction mixture under a stirring condition. The yellow coloured solution of the reaction mixture was immediately turned brown for both reactions. After 5-7 days, the microcrystalline brown coloured crystals for complexes **5** and **6** were separated from the reaction mixture upon slow evaporation in an open atmosphere that was dried over silica gel.

Yield of **L^4**: 0.230 g (~83.6%).

Yield of **5**: 0.2997 g (~81.0% metal salt based)

Yield of **6**: 0.289 g (~78.0% metal salt based).

6.2.2. Physical measurements

FT-IR spectra of the ligand and zinc complexes were recorded by a SHIMADZU spectrometer (FTIR-8400S) using a KBr pellet in the range of 400-3600 cm^{-1}. ^1H and ^{13}C NMR spectra of **L^4** and zinc complexes were obtained on a Bruker Advance 400 MHz spectrometer in $CDCl_3$ at 298 K. Steady-state absorption data were recorded with a HITACHI-U2910 spectrophotometer. ESI-MS spectral measurements were performed with a Q-TOF-micro quadruple mass spectrometer. A Perkin Elmer 2400 CHN microanalyser was employed to carry out the elemental analyses of the compounds.

Table 6.1. CHN analysis of the Schiff base ligand $\mathbf{L^4}$, zinc complexes **5** and **6**

Compound (Mol formula)	**Found (Calcd)%**		
	C	**H**	**N**
$\mathbf{L^4}$ **(**$C_{15}H_{15}NO_3$**)**	70.09 (70.02)	5.80 (5.88)	5.93 (5.44)
Complex 5 ($ZnC_{32}H_{30}N_4O_6S_2$**)**	55.37 (55.38)	4.07 (4.08)	4.07 (8.08)
Complex 6 ($Zn_2C_{30}H_{28}N_8O_6$**)**	49.54 (49.55)	3.88 (3.89)	15.41(15.42)

6.2.3. X-ray structural studies and refinement

A Rigaku XtaLABmini diffractometer equipped with Mercury 375R (2×2 bin mode) CCD detector was employed to collect X-ray diffraction data for the zinc(II) complexes with graphite monochromated Mo-Kα radiation (λ=0.71073 Å) at 296 K for complex **5** and 298 K for complex **6** using ω scans. The data were reduced using CrysAlisPro 1.171.39.35c, and the space groups were determined using Olex2. The crystal structures were resolved by the dual space method using SHELXT-2015. The crystallographic data were refined by full-matrix least-squares procedures using the SHELXL-2015 software package through the OLEX2 suite.[42-45]

6.2.4. Hirshfeld surface and energy framework analysis of the zinc complexes

Hirshfeld surfaces and 2D fingerprint plots for the zinc(II) complexes have been generated by Crystal Explorer 17.5 program package employing their X-ray diffraction data. The location of intermolecular interactions within crystal packing was examined through Hirshfeld Surface analysis. The details of Hirshfield surface analysis were described elsewhere.[46-48] The energy framework analysis was computed on Crystal Explorer 21.2 software (Turner et al., 2017, Mackenzie et al., 2017) with HF/3-21G basis sets using TONTO software for the cluster environment of 3.8 Å surrounding a particular molecule of interest. The total interaction energy was articulated as $E_{tot} = k_{ele}E'_{ele} + k_{pol}E'_{pol} + k_{disp}E'_{disp} + k_{rep}E'_{rep}$, where the k values belong to the scale factors for benchmarked energy models. E'_{ele} represents the electrostatic energy, E'_{pol} represents the polarisation energy, E'_{disp} represents the dispersion energy, and E'_{rep} represents the repulsive energy. To identify the interaction energies developed due to

supramolecular interactions, we set the tube dimension factor 300, where a greater tube radius is directly proportional to more substantial and prominent interaction.

6.2.5. Device construction and electrical conductivity under the photo- and dark conditions

Electrical measurements of **5** and **6** complexes-based devices were carried out in the dark chamber using HIOKI LCR Hi-Tester (Model No. 3532- 50) in the frequency range of 42 Hz to 5 MHz at room temperature. The complexes **5** and **6** were taken into powder form. These powder samples were pressed separately at a pressure of 200 kg/cm^2 in a palletizer to form circular pellets of thickness 10 mm and surface area 10 cm^2. Conductive silver paint was applied to two opposite sides of the pellets consisting of the complex to conduct electrical measurements. Here, the pellets of complexes **5** and **6** were referred to as device A and device B respectively. Further, devices A and B based on complexes **5** and **6** were also exposed to a 200 W electric bulb to get all electrical measurements data in the presence of a shower of photons.

6.2.6. Powder X-ray diffraction (PXRD) analysis

PXRD patterns of all the compounds were recorded on a Rigaku Ultima IV diffractometer using parallel beam geometry equipped with a Cu- Kα radiation, 2.5° Primary and secondary solar slits, 0.5° divergence slit with 10mm height limit slit, sample rotation stage (120 rpm) attachment and DTex Ultra detector. The tube voltage and current applied were 40kV and 40mA. The data were collected over an angle range of 5-80° with a scanning speed of 2° per minute with 0.01° step. The observed PXRD patterns have been compared using WINPLOTR[49] with the simulated PXRD patterns generated from the crystal coordinates using Mercury.

6.3. Results and discussion

6.3.1. Synthesis and formulation of

The reddish coloured Schiff base, **L^4** was synthesized by condensing *o*-anisidine with *o*-vanillin under reflux. The synthesis of **L^4** discussted in previous chapter V. The zinc complexes were successfully synthesized by reacting hydrated zinc perchlorate, **L^4** and pseudohalides in 1:2:2 stoichiometry at room temperature under an aerobic atmosphere. Perhaps, we tried different stoichiometry and combinations of the reactants with a variation of solvents. Still, we successfully isolated the zinc(II) complexes with 1:2:2

stoichiometry of the reactants in methanol (**Scheme 6.1**). A variation of zinc(II) salts like chloride, bromide, acetate, nitrate and sulphate have also been combined with **L**[4] and pseudohalides to understand the structural diversity. Although, we have synthesised the zinc complexes in the polycrystalline phase with various zinc(II) salts. Zinc perchlorate was the most effective salt to prepare the complexes **5** and **6** in the form of single crystals. The complexes were soluble in common solvents like methanol, acetonitrile, dichloromethane etc.

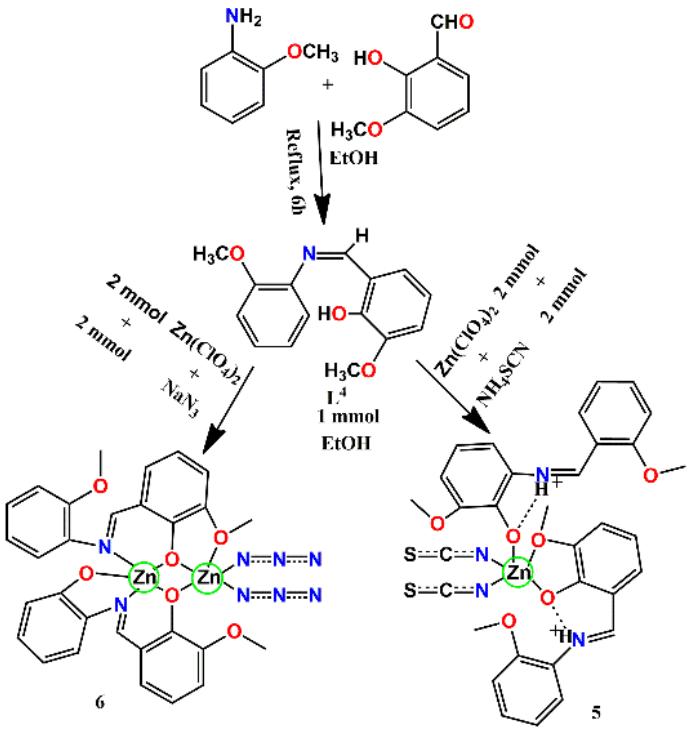

Scheme 6.1. Synthetic route for the formation of zinc complexes **5** and **6**

6.3.2. Infrared spectral analysis

The zinc complexes **5** and **6** were characterized by FT-IR spectra (**Fig. 6.2**). The complex **5** showed strong and sharp characteristic peaks at 2028 and 1628 $cm^{-1,}$ while complex **6** displayed high intensity strong peaks at 2073 and 1610 cm^{-1} which can be assignable to the presence of coordinated pseudohalides and azomethine groups, respectively (**Fig. 6.2**). The observed peaks for the coordinated functional groups to the metal centre agree with the literature values.[51,52] The closely-spaced stretching frequencies of the zinc complexes in the region 1650-500 cm^{-1} indicate the existence of (Ar)C–O, (Ar)C–C, (Ar)C–O, (Ar)–OCH_3, Zn–O(Ar), Zn–N(imine) and others (**Fig. 6.2**).

Table 6.2. Infrared spectral data[a]

Compounds	ν (cm^{-1})	Functional groups
L^4	3432, 1614	–OH, –C=N–
Complex 5	2028, 1628	–N=C=S, –C=N–
Complex 6	2073, 1610	–N_3, –C=N–

[a]KBr disc

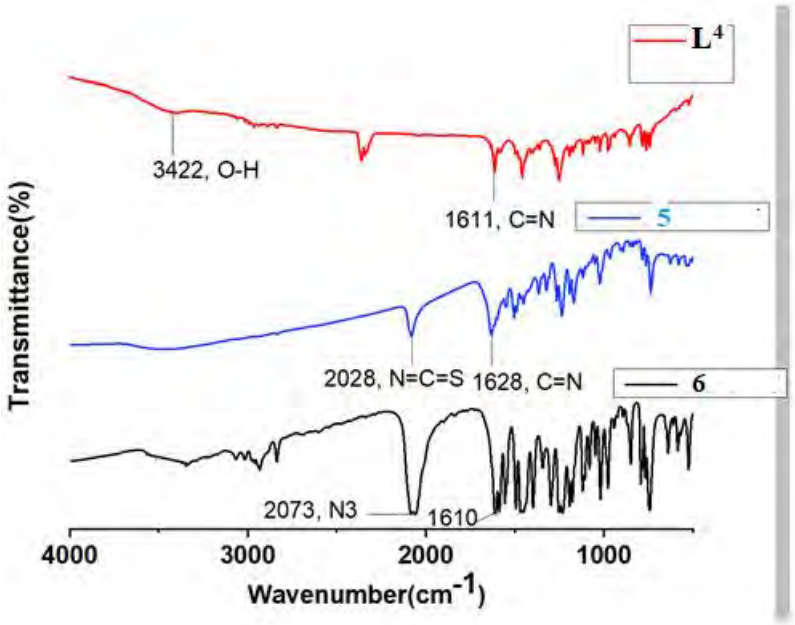

Fig. 6.1 FT-IR spectrum of the Schiff base **L^4**, zinc complexes **5** and **6**

6.3.3. Electronic spectral analysis

The electronic spectra were recorded in methanol at room temperature to understand the solution behaviour of the zinc complexes (**Fig. 6.2**). The complex **5** displayed the electronic bands in methanol at 224, 270, 335 and 419 nm. The appearance of bands at 224 and 270 nm corresponds to π→π* / n→π* electronic transitions of **L^4** ligand while the optical bands at 370 and 419 nm attribute the charge transfer transition (**Fig. 6.2**). In contrast, the complex **6** showed the electronic bands at 277, 340 and 436 nm in methanol. The higher energetic band at 277 nm was assignable to π→π* / n→π* electronic transitions of ligand origin, and the lower energetic bands attribute the charge transfer transition. The observed electronic bands were in good agreement with previously reported values.[53,54]

Table 6.3. UV-Vis spectral data[b]

Compounds	λ_{max}, nm
Complex 5	270 (0.17), 335 (0.16), 419 (0.045)
Complex 6	277 (0.41), 340 (0.59), 436 (0.19)

[b]methanol solution at 298K

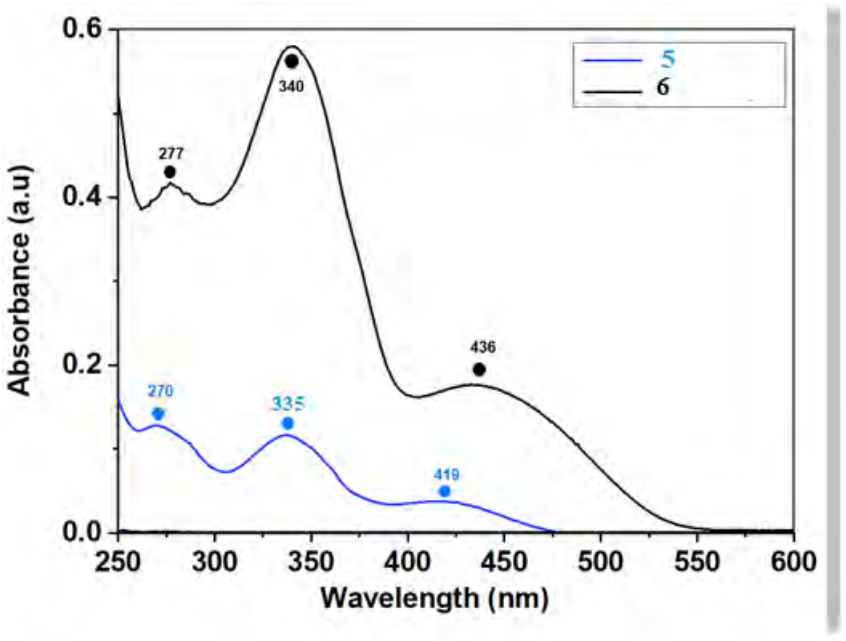

Fig. 6.2. UV-Vis spectrum of the Zn (II) complexes **5** and **6** in MeOH medium

6.3.4. ^{1}H NMR spectral analysis

The ^{1}H NMR spectra of complexes **5** and **6** were recorded in $CDCl_3$ at room temperature (**Fig. 6.3** and **Fig. 6.4**). The **5** complex displayed a characteristic peak at 9.94 ppm assigning the zwitterionic proton attached to azomethine-N. The proton attached to azomethine-C showed a proton signal at 8.83 ppm for complex **5**. The proton signals corresponding to aromatic-C appeared in the range 7.34 to 6.84 ppm while the -OCH_3 protons were marked at ~3.9 ppm. In contrast, the azomethine proton of complex **6** showed a characteristic signal at 8.74 ppm. The complex **6** displayed the aromatic proton signals in between 7.29 to 6.86 ppm and the methoxy-protons appeared at ~3.93 ppm. The appearance of the proton signals for both the complexes confirmed the structural characterization of the compounds to a great extent.

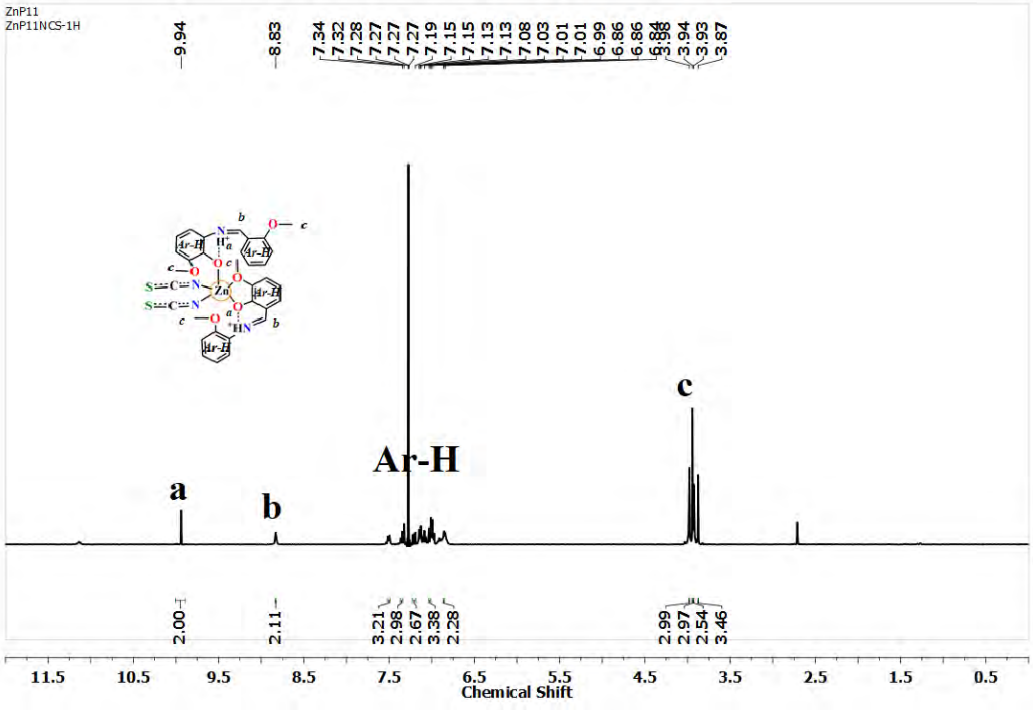

Fig. 6.3. ^{1}H NMR spectrum of **5**

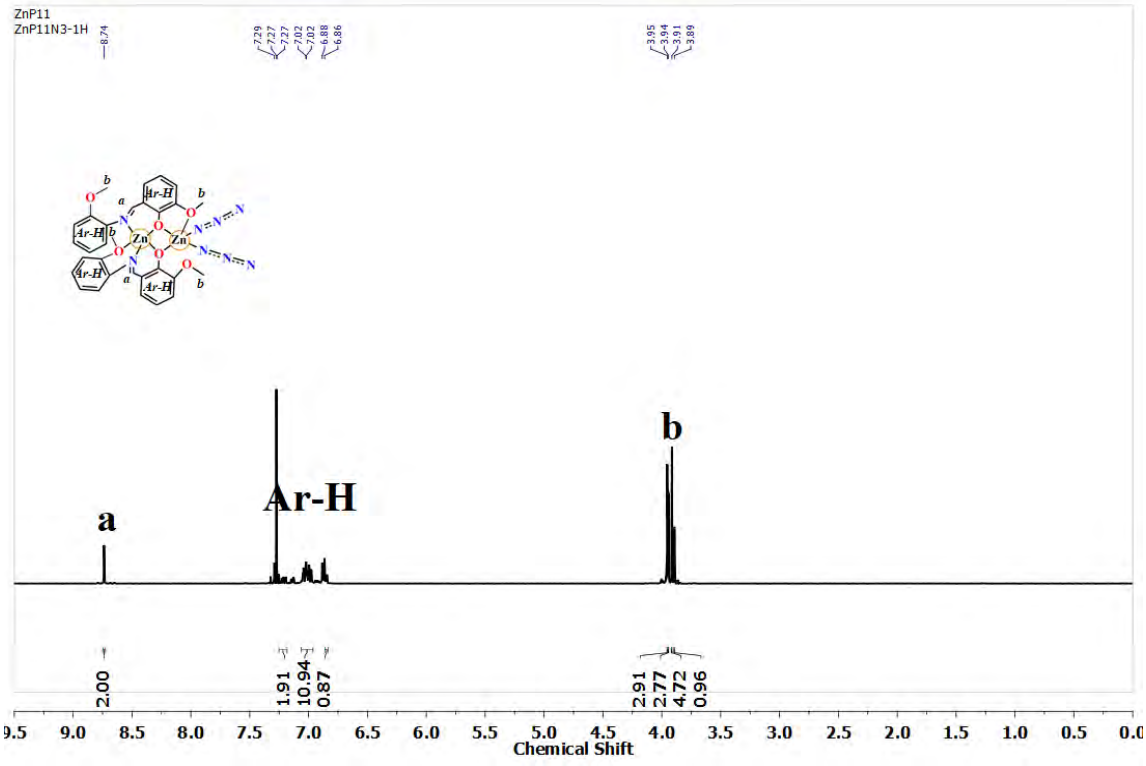

Fig. 6.4. ^{1}H NMR spectrum of **6**

6.3.5. Description of crystal structure and supramolecular interactions

Crystal structure analysis revealed that the zinc complexes, **5** and **6** crystallize in monoclinic and orthorhombic systems with *C2/c* and *P*bca space groups, respectively. The thermal ellipsoidal plots of the zinc complexes were shown in **Fig. 6.5a** and **Fig. 6.6a**. The crystal structure refinement parameters for the zinc complexes were summarized in **Table 6.4**.

Table 6.4. The crystal structure refinement parameters for the zinc complexes

Parameters	**5**	**6**
CCDC Number	2120412	2120413
Empirical	$ZnC_{32}H_{30}N_4O_6S_2$	$Zn_2C_{30}H_{28}N_8O_6$
Formula weight	696.09	727.34
Temperature (K)	296	298
Crystal system	Monoclinic	Orthorhombic
Space group	*C2/c*	*P*bca
a (Å)	32.3897(8)	15.9766(2)
b (Å)	10.8311(4)	16.8420(3)
c (Å)	18.4897(7)	22.9222(4)
Volume ($Å^3$)	6486.1(4)	6167.86(17)
Z	8	8
ρ (gcm^{-3})	1.426	1.567
μ (mm^{-1})	0.935	1.613
F (000)	2880	2976
Index ranges	-46 :48; -16: 16; -28: 22	-23: 24; -25: 23; -34: 32
θ ranges (º)	2.5-32.8	2.5-32.8
Total reflections	45356	69383
Unique reflections	11348	11161
R_1 [I > 2σ(I)]	0.0514	0.0452
R_{int}	0.033	0.040
wR_2 (all data)	0.1734	0.1419
GooF	1.01	1.03
Largest peak and hole ($eA^{\circ-3}$)	-0.36, 0.69	-0.67, 0.50

Weighting Scheme: $R= \Sigma|Fo|-|Fc||/\Sigma|Fo|$, $wR2=[\Sigma w(Fo^2-Fc^2)^2/\Sigma w(Fo^2)^2]^{1/2}$, Calc. $w = 1/[\sigma^2(Fo)^2 + (0.0775P)^2+ 2.4387P]$ (**5**); where $P = (Fo^2+2Fc^2)/3$.

Calc. $w = 1/[\sigma^2(Fo)^2 + (0.0678P)^2+ 1.4852P]$ (**6**); where $P = (Fo^2+2Fc^2)/3$.

The zinc(II) ion centric bond distances and bond angles of complexes **5** and **6** were given in **Table 6.5** and **Table 6.6**. The Schiff base, $\mathbf{L^4}$ behaved differently in the formation of zinc complexes in the crystalline phase. The ligand adopted an interesting zwitterionic form in the structure of complex **5**, restricting a limit on the tetradenticity of the ligand. In contrast, $\mathbf{L^4}$ behaved as a suitable tridentate chelating ligand with symmetric $\mu_{1,1}$-bridging motif through phenoxo ion in the crystal structure of complex **6**. Indeed, the Schiff base ligand was designed as a tetradentate chelator following the principle of thermodynamics; however, in reality, the ligand turned out to be tridentate and bidentate/monodentate ligand towards a zinc(II) ion in the presence of pseudohalides.

Table 6.5. Bond distances and bond angles for the complex **5**

Bond lengths (Å)			
Zn1–O1	2.422(2)	Zn1–O2	1.9798(17)
Zn1–O5	1.9975(17)	Zn1–N1	1.993(3)
Zn1–N2	21.988(2)		
Bond angles (°)			
O1–Zn–O2	73.33(7)	O1–Zn1–O5	81.57(7)
O1–Zn–N1	84.18(11)	O1–Zn1–N2	168.92(10)
O2–Zn–O5	138.31(7)	O2–Zn1–N1	103.82(10)
O2–Zn–N2	102.00(9)	O5 –Zn1–N1	106.16(9)
O5–Zn1–N2	96.35(9)	N1–Zn1 –N2	106.80(10)

Table 6.6. Bond distances and bond angles for the complex **6**

Bond lengths (Å)			
Zn1–O1	1.9869(15)	Zn1 –O2	2.0094(16)
Zn1–O3	2.3827(17)	Zn1 –O6	2.6041(17)
Zn1–N1	2.0189(18)	Zn1 –N2	2.0440(18)
Zn2 –O1	2.0541(16)	Zn2 –O2	2.0772(16)
Zn2 –O4	2.6605(19)	Zn2 –O5	2.5506(17)
Zn2 –N3	1.962(2)	Zn2 –N6	1.942(3)
Bond angles (°)			
O1 –Zn1 –O2	78.57(7)	O1 –Zn1 –O3	132.49(6)
O1 –Zn1 –O6	88.65(6)	O1 –Zn1 –N1	138.85(7)
O1 –Zn1 –N2	90.15(7)	O2 –Zn1 –O3	90.65(6)
O2 –Zn1 –O6	129.25(6)	O2 –Zn1 –N1	91.27(7)
O2 –Zn1 –N2	143.98(7)	O3 –Zn1–O6	130.47(6)

O3–Zn1 –N1	86.78(6)	O3 –Zn1 –N2	71.97(6)
O6 –Zn1 –N1	67.19(6)	O6 –Zn1 –N2	83.87(6)
N1 –Zn1–N2	118.03(8)	O1 –Zn2 –O2	75.54(6)
O1 –Zn2 –O4	65.32(6)	O1 –Zn2 –O5	141.05(6)
O1 –Zn2 –N3	110.88(9)	O1 –Zn2 –N6	112.36(9)
O2 –Zn2 –O4	139.60(6)	O2 –Zn2 –O5	66.40(6)
O2 –Zn2 –N3	102.39(8)	O2 –Zn2 –N6	118.52(9)
O4 –Zn2 –O5	153.58(6)	O4 –Zn2 –N3	83.29(8)
O4 –Zn2 –N6	86.62(9)	O5 –Zn2 –N3	85.79(8)
O5 –Zn2 –N6	80.47(9)	N3 –Zn2 –N6	125.94(11)

The X-ray structural analysis of the complex **5** indicated that the Zn(II) ion adopted a square pyramidal coordination geometry. The complex existed in a cisoid conformation to thiocyanate ions (**Fig. 6.5a**). Two units of the zwitterionic ligands and two thiocyanate ions facilitate the formation of the square pyramidal geometry. The square plane consists of two phenoxy-O and one methoxy-O of the coordinated ligand along with a coordinated thiocyanate ion. The second thiocyanate coordinates axially with the zinc(II) centre and satisfies the square pyramidal geometry of **5** (**Fig. 6.5a**). Three of the four methoxy groups attached to the Schiff base backbone remain non-reactive in forming the complex **5**. The formation of the square plane was further evident from the average bond angle value around the zinc centre as ∠L–Zn–L, 88.30º (**Table 6.5**). The terminally coordinated thiocyanate ions maintain a high degree of linearity in their coordination to the zinc ion in complex **5**.

The crystal structure analysis of the complex **6** revealed that the zinc centres (Zn1, Zn2) existed in square pyramidal coordination geometries (**Fig. 6.6a**). The zinc centres were interconnected through $\mu_{1,1}$-type phenoxo-bridges of the Schiff base ligands with an internuclear distance of 3.17 Å. The bridging angles were determined as ∠Zn1-O1-Zn2, 103.53° and ∠Zn1-O2-Zn2, 101.96° (**Table 6.6**). In forming the dinuclear zinc complex, the Schiff base acts as a tridentate chelator. The coordination environment around the zinc centres (Zn1 and Zn2) was entirely different. The square plane of Zn1 consists of the oxygen (O1 and O2) of phenoxo-bridges, O3 of methoxy-O and azomethine-N (N2). In contrast, the square plane of Zn2 centres was formed by the coordination of the oxygen (O1 and O2) of phenoxo-bridges, O5 of methoxy-O and

azide-N (**Fig. 6.6a**). The average bond angle value for the square plane around Zn1 and Zn2 centres were estimated to be ∠L–Zn1–L, 82.83º and ∠L–Zn2–L, 88.69º (**Table 6.6**). The azide ions make terminal coordination to the Zn2 centre and maintain a high degree of linearity ∠N–Zn2–N, 176.1º.

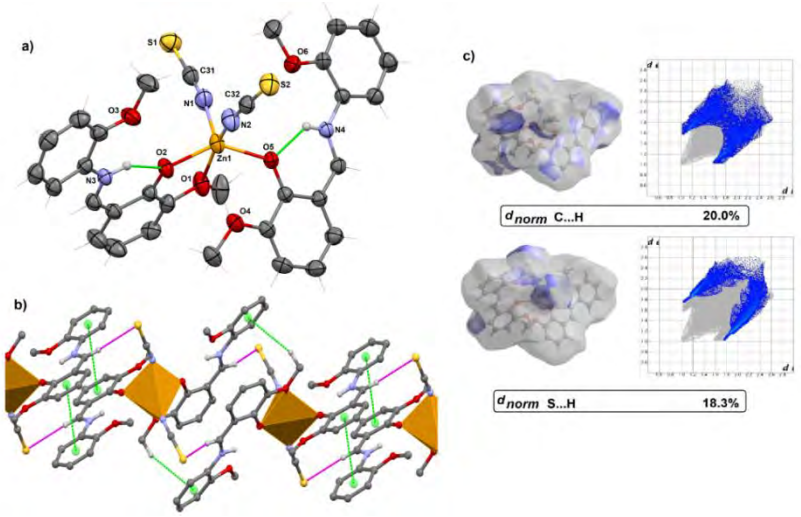

Fig. 6.5. (a) Thermal ellipsoid plots of **5**; (b) 1D supramolecular framework of **5**; (c) Hirshfeld surface and 2D fingerprint plots

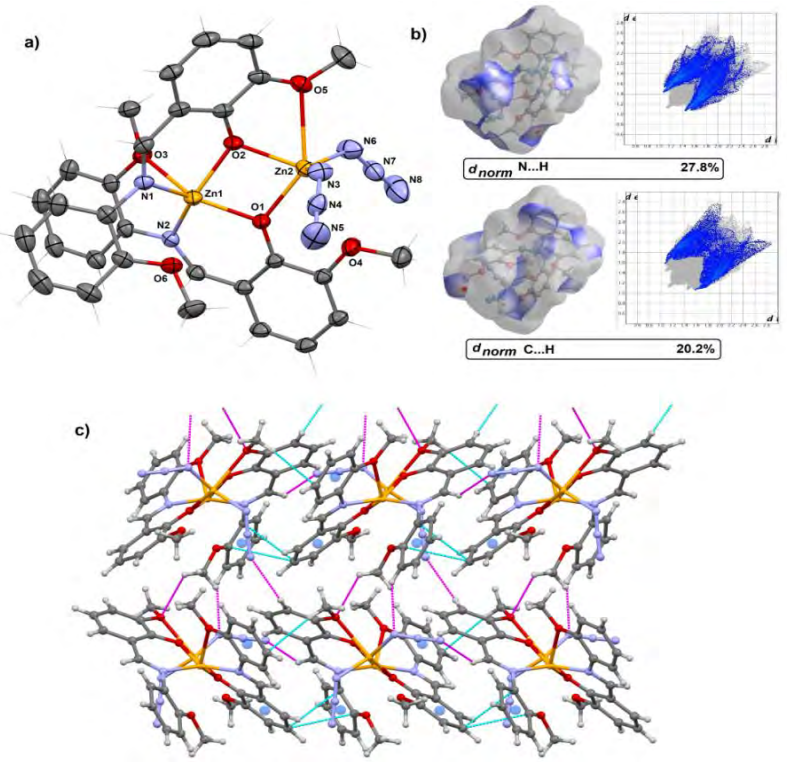

Fig. 6.6. (a) Thermal ellipsoid plots of **6**; (b) Hirshfeld surface and 2D fingerprint plots; (c) 3D supramolecular architecture of **6**

The differentiation in the structural composition and formation of zinc complexes under a similar reaction condition may be explained in terms of the Lewis acidity of the zinc ion. The reaction condition was kept identical for the synthesis of complexes **5** and **6**. Azide and thiocyanate were the pseudohalides that were considered linear homo- and hetero-atomic molecular rods, respectively. It was well known that NCS^- consists of a terminal S-atom and can exist in different resonating structures. Owing to a vacant 3d-orbital of S, it may cause a retardation in the Lewis acidic behaviour of zinc, and consequently, a lesser Lewis acidity of the zinc ion cannot strongly compensate the Lewis basicity of the Schiff base, leading to the existence of a zewitter ionic form of the Schiff base.[55] In contrast, the azide ion consists of all the N-donors that do not have the d- orbital. Consequently, the strong Lewis acidity of the zinc centre imposes excellent attraction towards the coordination environment supplied by the Schiff base. Further, the steric factor of the co-ions may have some critical role in the formation of the different structural compositions of the zinc complexes.[56]

To explain the peculiar behaviour of a polydentate Schiff base, we developed the single crystals of the Schiff base ligand and explored its supramolecular architecture. The asymmetric unit of the ligand crystallizes in the orthorhombic system and exists in a Z-stereomer. The phenolic-OH keeps a strong intramolecular hydrogen bonding with the N of azomethine. The methoxy-O makes an intermolecular H-bonded network with the H attached to the carbon atom of phenyl and grows in a 3D architecture in *ac* plane. We also explored the self-assembled supramolecular frameworks for zinc complexes. The complex **5** formed a beautiful 1D crystalline architecture through a short-ranged intermolecular C− H···S hydrogen bonding and C− H···π interactions (**Fig. 6.5b**). In contrast, complex **6** displayed the active participation of dominant intermolecular N− H···N hydrogen bonding and C− H···π interactions leading to a 3D crystalline architecture (**Fig. 6.6b**).

6.3.6. Hirshfeld surface and energy framework analysis

The Hirshfeld surface analysis of the zinc complexes was further carried out to comprehend the contribution of supramolecular interactions. The complexes' Hirshfeld surface analysis plots were shown in **Fig. 6.7 and 6.8**. The surface volume of the complexes **5** and **6** were calculated as 799.97 and 761.83 $Å^3$, respectively, while the surface areas were estimated to be 624.15 and 570.82 $Å^2$, respectively. The degrees of non-covalent interactions of **5** and **6** were revealed from the 2D fingerprint plots

between d_e and d_i (**Fig. 6.5C and 6C**). It was evident from the Hirshfeld surface calculations of complex **5** that intermolecular S···H bonding (18.3%) and C–H···π interaction (20.0%) contribute nearly 38% of total Hirshfeld surface displaying an influential sharp tooth in fingerprint plots (**Fig. 6.5C**).

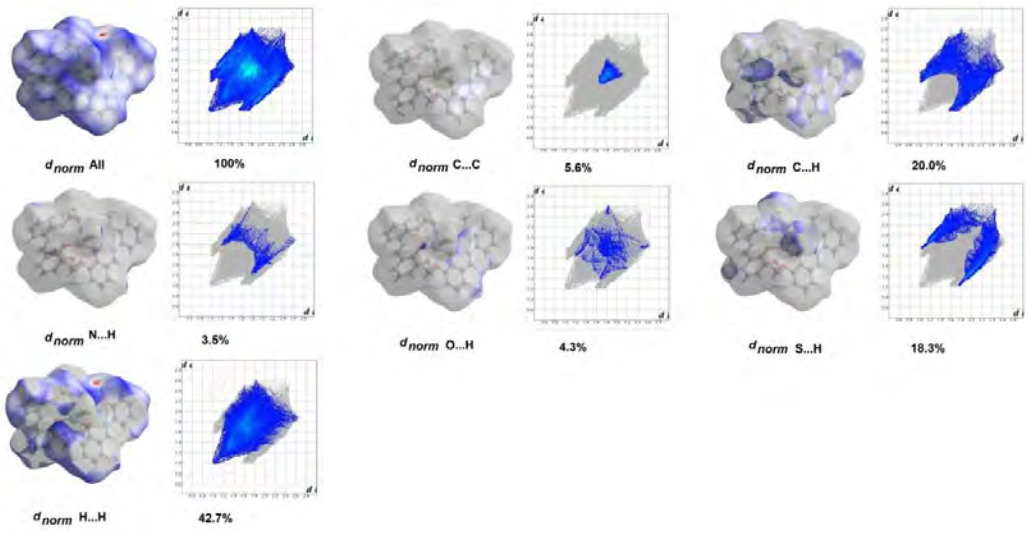

Fig. 6.7. Hirshfeld surface analysis plots of complex **5**

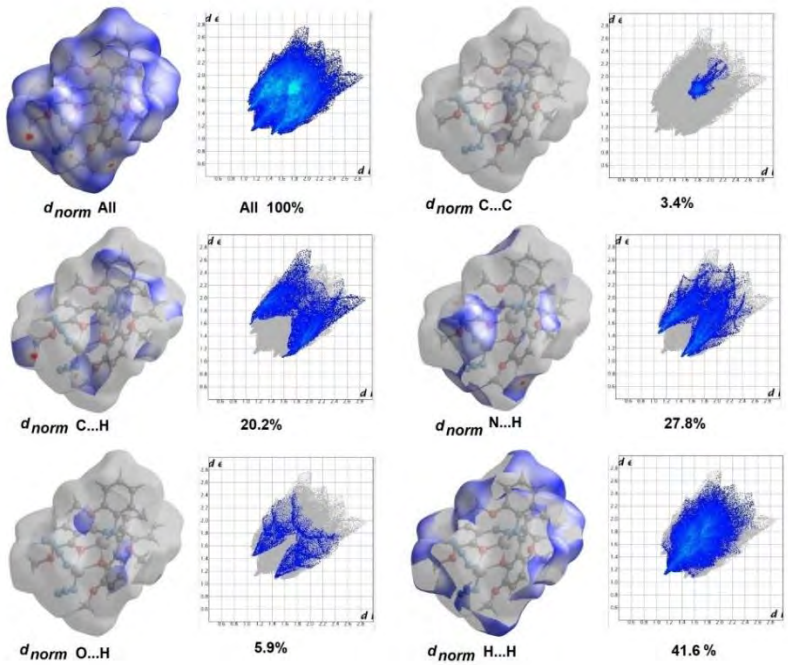

Fig. 6.8. Hirshfeld surface analysis plots of complex **6**

In contrast, Hirshfeld surface calculations of **6** revealed that intermolecular N···H bonding (27.8%) and C–H···π interaction (20.2%) make a considerable coverage

(~48%) of the total surface. The π···π interaction has less than 6% of Hirshfeld surface coverage for both the zinc complexes. The presence of sharp teeth from fingerprint plots represented the dominant intermolecular hydrogen bonding interactions in both the **5** and **6** complexes i.e. a high contribution from the Coulumb energy parameter was evident in total energy expression. The C–H···π interactions play a pivotal role in developing the long-range supramolecular crystal architecture of the zinc complexes as revealed from the large contribution of dispersive force over the coulombic force in energy framework analysis (**Fig. 6.9 and 10**).

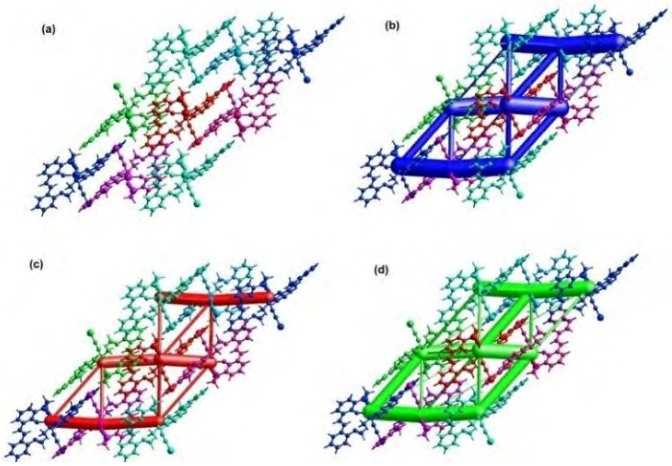

Fig. 6.9. (a) Energy framework diagram, (b) total energy plot, (c) coulomb energy contribution plot, and (d) dispersive energy contribution plot mapped for complex **5**

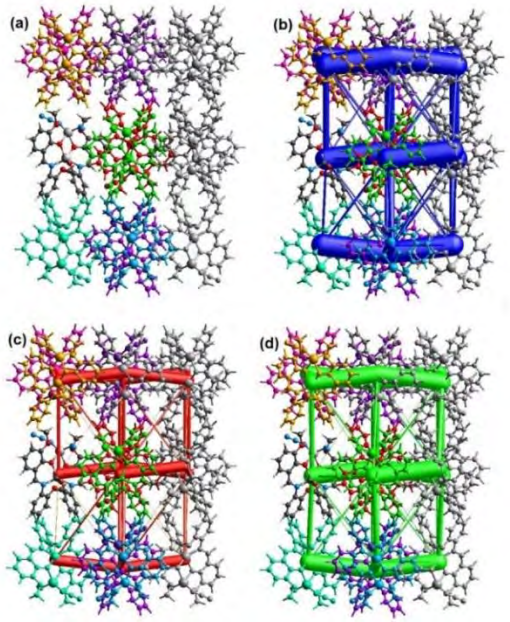

Fig. 6.10. (a) Energy framework diagram, (b) total energy plot, (c) coulomb energy contribution plot, and (d) dispersive energy contribution plot mapped for complex **6**

The predominance of dispersive forces for both the zinc complexes was justified by the greater inner dimension of green cylinders than red cylinders between the same molecules (**Fig. 6.9.** and **6.10.**). In the complex **5**, the total electrostatic energy (-255.2 kJ/mol) and total dispersive energy (-498.4 kJ/mol) played a significant role in the molecular stabilization of the complex, as evident from the calculated total energy (-484.6 kJ/mol) from the energy framework analysis. In comparison, the polarisation energy (-24.4 kJ/mol) contributed a little to the total energy of complex **5** (**Table 6.7**).

Table 6.7. Contribution of different energy components to the stabilisation of molecular frameworks for complex **5**

	N	Symop	R	Electron Density	E_ele	E_pol	E_dis	E_rep	E_tot
	2	x, y, z	10.83	B3LYP/6-31G(d,p)	-9.5	-2.9	-26.1	22.6	-21.0
	1	-x, -y, -z	16.25	B3LYP/6-31G(d,p)	1.3	-0.3	-1.3	0.0	0.0
	1	-x, -y, -z	8.40	B3LYP/6-31G(d,p)	-85.4	-1.0	-130.9	107.9	-138.4
	2	x, -y, z+1/2	9.89	B3LYP/6-31G(d,p)	-23.9	0.0	-25.0	11.7	-39.8
	1	-x+1/2, -y+1/2, -z	8.78	B3LYP/6-31G(d,p)	-82.6	-0.5	-133.1	100.9	-141.3
	2	x, -y, z+1/2	11.79	B3LYP/6-31G(d,p)	-2.4	-6.1	-11.5	11.0	-10.3
	1	-x, y, -z+1/2	11.81	B3LYP/6-31G(d,p)	-20.5	0.0	-91.0	61.0	-63.2
	2	x+1/2, -y+1/2, -z+1/2	18.83	B3LYP/6-31G(d,p)	0.8	-0.6	-6.3	2.8	-3.4
	1	-x+1/2, -y+1/2, -z+1/2	12.38	B3LYP/6-31G(d,p)	7.5	-1.1	-20.0	5.7	-6.8
	2	-x+1/2, y+1/2, -z+1/2	13.99	B3LYP/6-31G(d,p)	1.2	-2.5	-24.1	10.0	-15.4
	1	-x, -y, -z	10.57	B3LYP/6-31G(d,p)	-21.2	-9.4	-29.2	15.9	-45.0

Energy Model	k_ele	k_pol	k_disp	k_rep
CE-HF ... HF/3-21G electron densities	1.019	0.651	0.901	0.811
CE-B3LYP ... B3LYP/6-31G(d,p) electron densities	1.057	0.740	0.871	0.618

In contrast, the total electrostatic energy, total dispersive energy and polarisation energy in complex **6** were estimated to be -126.8 kJ/mol, -304.8.4 kJ/mol and -50.6 kJ/mol, respectively, which caused a significant contribution to the stabilization of the molecular framework as revealed from the calculated total energy (-314.7 kJ/mol) by energy framework analysis (**Table 6.8**). It was observed that the electrostatic, polarisation and dispersive energies contributed a dominant role for complex **5** relative to complex **6** and developed an extensive binding force in the molecular frameworks of complex **5**.

Table 6.8. Contribution of different energy components to the stabilisation of molecular frameworks for complex **6**

	N	**Symop**	**R**	**Electron Density**	**E_ele**	**E_pol**	**E_dis**	**E_rep**	**E_tot**
	1	x+1/2, y, -z+1/2	7.99	B3LYP/6-31G(d,p)	- 63.7	- 21.8	- 119.9	84.3	-135.8
	1	x, -y+1/2, z+1/2	12.10	B3LYP/6-31G(d,p)	- 19.4	- 4.1	-3 3.3	23.5	-38.0
	0	-x, y+1/2, -z+1/2	8.44	B3LYP/6-31G(d,p)	- 36.2	0.0	- 71.8	49.0	-70.5
	2	-x+1/2, y+1/2, z	11.30	B3LYP/6-31G(d,p)	- 3.9	- 7.0	- 15.2	11.0	-15.7
	1	-x, -y, -z	12.13	B3LYP/6-31G(d,p)	3.1	0.0	- 33.7	18.9	-14.4
	1	x+1/2, -y+1/2, -z	14.33	B3LYP/6-31G(d,p)	2.4	- 8.9	- 8.5	3.0	-9.6
	0	-x+1/2, -y, z+1/2	14.94	B3LYP/6-31G(d,p)	- 8.5	0.0	- 4.4	1.6	-11.8
	2	-x+1/2, -y, z+1/2	14.45	B3LYP/6-31G(d,p)	- 1.1	- 8.8	-2.9	0.0	-10.2

	1	-x, -y, -z	12.54	B3LYP/6-31G(d,p)	0.5	0.0	-15.1	6.2	-8.7

Energy Model	k_ele	k_pol	k_disp	k_rep
CE-HF ... HF/3-21G electron densities	1.019	0.651	0.901	0.811
CE-B3LYP ... B3LYP/6-31G(d,p) electron densities	1.057	0.740	0.871	0.618

6.3.7. Dark- and photo-electrical conductivities studies

AC conductivity spectra in the dark chamber (dark-conductivity) as well as in the presence of a shower of photons (photoconductivity) of complex **5** were presented in **Fig. 6.11a**. It was evident from **Fig. 6.11a** that a plateau region (frequency-independent) was observed at low frequency attributing to the photo-activated nature of device A. The plateau region at low frequencies corresponds to DC conductivity, which was found to be smaller for photo-conductivity conditions. However, a dispersion in AC conductivity has been observed in the higher frequency region (**Fig. 6.11a**) which may occur due to the correlated motion of electrons.[56,57] The crossover region between DC conductivity and AC conductivity implies the "start of dispersion", corresponding to the crossover or hopping frequency.[56-58]

In contrast, the AC conductivity spectral analysis of complex **6** in the dark and photo condition of complex **6** revealed a constant conductivity over a wide range of frequencies at room temperature. The conductivity spectrum of device B was shown in **Fig. 6.12a**. The nature of spectra corresponds to DC conductivity with a less interactive frequency zone between electron and crystal lattice. In this case, the interaction starts at a high frequency and consequently resistivity sharply increases at a particular frequency (crossover frequency). This feature was suitable for template application because the deposited film onto this sample will get a constant resistance region.[59] It iwas also observed that photoconductivity increases sharply to its dark-conductivity to almost one order in the conductivity scale as shown in **Fig. 6.12a**. Literature survey suggests that the mechanism of limiting the mobility of charge carriers at a higher degree may be considered due to optical phonon-assisted hopping of electrons.[56, 57]

It was well known that electrode polarization effects[48-50] in dielectric spectra may cause difficulty in the computation of various dielectric parameters, particularly at low frequencies. Efforts[56-58] have been made in the past to correct the electrode polarization

effect. Electric modulus formalism can be used for investigating the complex electrical response of a system by nullifying the electrode polarization effect as the reciprocal of complex permittivity was taken into account. The complex electrical modulus can be presented as[56-58]:

$$M^* = \frac{1}{\varepsilon^*} = M^{/} + j\,M^{//} = \frac{\varepsilon^{/}}{(\varepsilon^{/})^2+(\varepsilon^{//})^2} + j\,\frac{\varepsilon^{//}}{(\varepsilon^{/})^2+(\varepsilon^{//})^2} \qquad \textbf{(6.1)}$$

where, M* was the complex modulus, ε* was the complex dielectric permittivity, $M^{/}$ was the real and $M^{//}$ was the imaginary parts of the electric modulus.

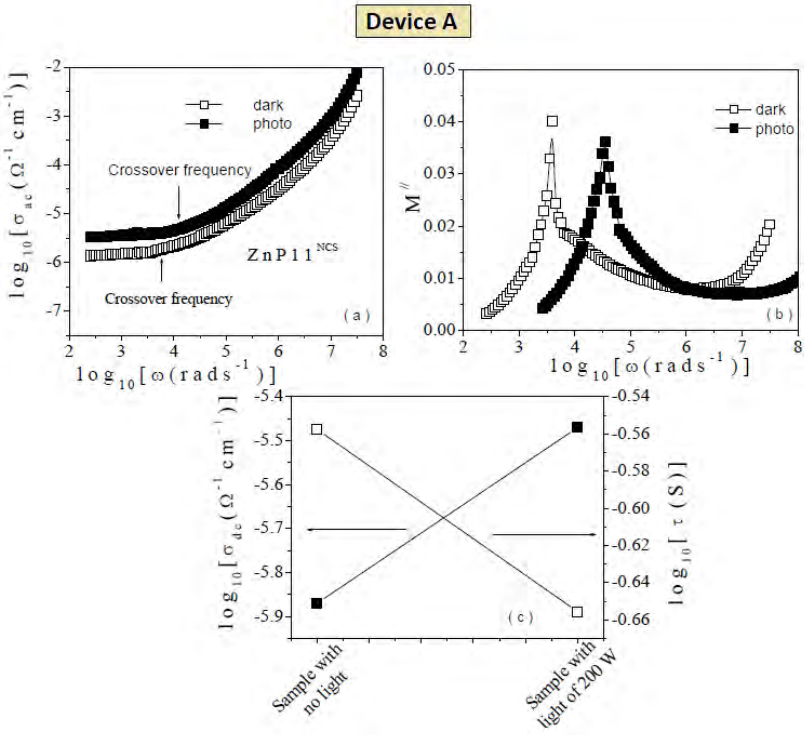

Fig. 6.11. (a) Conductivity Spectra, (b) electric modulus spectra and (c) room temperature DC conductivity and relaxation time for dark and photo conditions of complex **5**

The description of the electric modulus spectra of the present devices (A and B) in a wide frequency and temperature range may compel us to explore complete dielectric properties. **Fig. 6.11(b)** and **Fig. 6.12(b)** illustrates $M^{//}$ spectra at room temperature for device A complex **5** and device B complex **6**. The dielectric loss peak in **Fig. 6.11(b)**. helped us to estimate relaxation times. It can also be seen from **Fig. 6.11(b)** that at low frequency region, $M^{//}$ approaches to zero, which implies the suppression of electrode polarization effect. At higher frequencies, the impact of the relaxation process makes $M^{//}$ maximum.[51] As the frequency increases, $M^{//}$ was found to decrease, which may

suggested the short-range mobility of charge carriers in the system. It was evident from **Fig. 6.11(b)** that $M^{//}$ peaks have been shifted towards higher frequency region as we move from dark-conductivity to photoconductivity phenomena. This was an indication of the optical phonon activated relaxation process in the system. $M^{//}$ peak positions in **Fig. 6.11(b)**. corresponds to peak relaxation frequency (ω_{max}). In this approximation[56-58], ω_{max} indicates the limiting frequency up to which the charge carriers (electrons/ polarons) may hop over long distances. Beyond ω_{max} region, charge carriers were supposed to be confined to potential wells, where they are freely accessible. It may be concluded from this discussion, that the transition of mobility of charge carriers from long range to short range order takes place at ω_{max}. To analyse the nature conduction mechanism, it was approximated that the present systems undergo Debye type relaxation[56-58], which requires the essential condition: $\omega_{max} \times \tau = 1$, where, τ is the relaxation time. The estimated DC conductivity, as well as relaxation time τ with respect to dark and photoconductivity conditions, are projected in **Fig. 6.11(c)**. respectively. As the sample exposes to photons, τ was found to decrease. It should also be pointed out that nature of variation of τ can be validated from the nature of DC conductivity as presented in **Fig. 6.11(c)**.

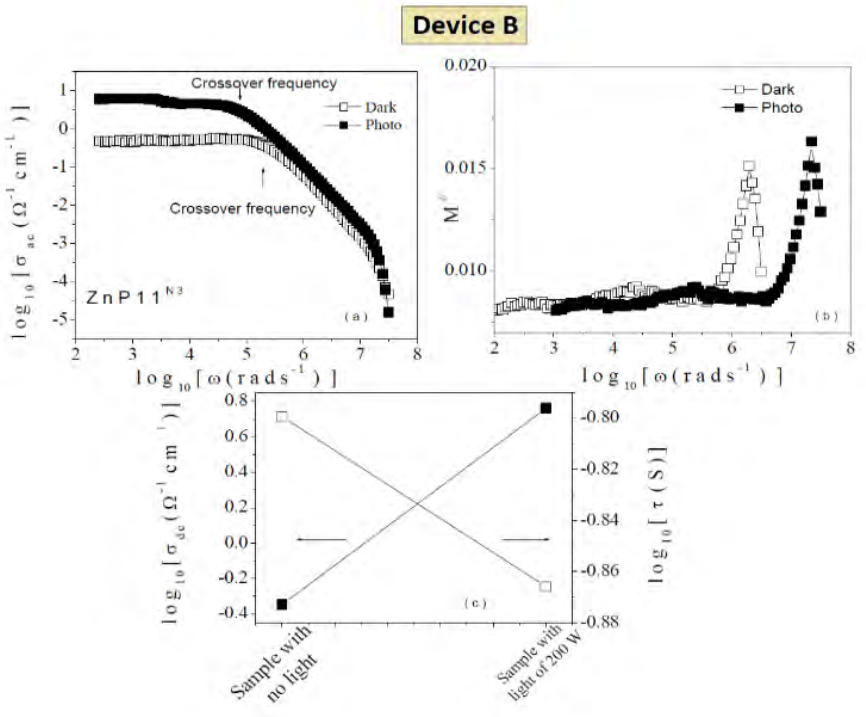

Fig. 6.12. (a) Conductivity Spectra, (b) electric modulus spectra and (c) room temperature DC conductivity and relaxation time for dark and photo conditions of complex **6**

It was also clear from the comparative study of **Fig. 6.11**(**b**) and **Fig. 6.12**(**b**) that relaxation frequency for device A was much less compared to that for device B. This result indicates that the relaxation process starts quickly for **5**, which may arise a question of the high stability of complex **5**. Estimated values of DC conductivity and relaxation times for device B were presented in **Fig. 6.12**(**c**), which was similar to those as presented in **Fig. 6.11**(**c**) of complex **5**. The only difference was that room temperature DC conductivity for device A was much less than that for device B. But at the same time, the relaxation times for device A was higher than that for device B, which was a good indication for the stability of the said system under study. Numerical values of room temperature DC Conductivity and relaxation time for device A were estimated to be $1.32 \times 10^{-6}\ \Omega^{-1}\ cm^{-1}$ and 0.310 S at the dark condition and $3.20 \times 10^{-6}\ \Omega^{-1}\ cm^{-1}$ and 0.224 S at photo condition, respectively. In contrast, numerical values of above-mentioned estimations for device B were 0.41 $\Omega^{-1}\ cm^{-1}$ and 0.210 S at dark condition and 6 $\Omega^{-1}\ cm^{-1}$ and 0.134 S at photo condition, respectively. This result directly indicated that device B showed much higher conductivity at dark as well as photo conditions than that of device A. It was apprehended to predict the optical phonon frequency (ν_0) from first absorption peak of IR vibration spectra[51] using the relation: $c = \lambda\nu_0$, where $c = 3 \times 10^{10}$ (cm/s), ν_0 was the optical phonon frequency (Hz), λ was the wavelength (cm). The Debye temperature (θ_D) of the present devices (A and B) could be estimated using the relation: $h\nu_0 = K_B\theta_D$, where h was the Plank's constant and K_B was Boltzmann constant. The computed values of optical phonon frequency and Debye temperature from the first absorption peak of IR vibration spectra are found to be $2.4 \times 10^{13}\ S^{-1}$ and 1150 K for device A and $1.5 \times 10^{13}\ S^{-1}$ and 720 K for device B, respectively (**Fig. 6.13**).

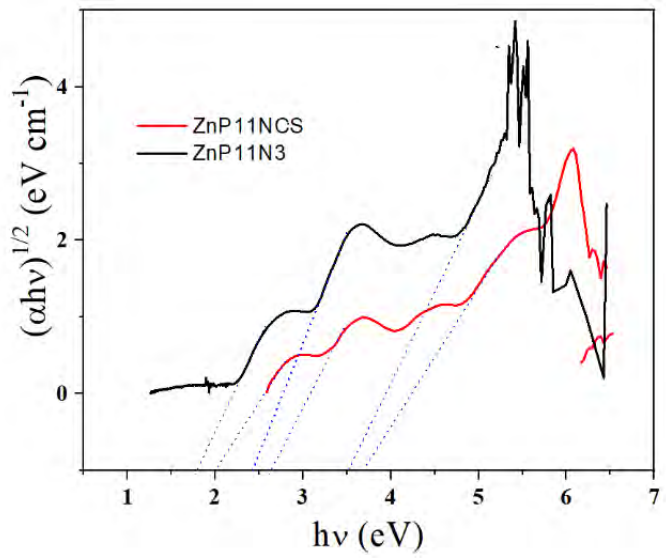

Fig. 6.13. Tauc plots of the zinc complexes

Debye temperature can be regarded as the limit defining the stability of the lattice. It may be considered that electrons/ polarons move across the lattice planes with minimal scattering (low electron/ polarn-phonon coupling). Above the Debye temperature, the scattering becomes quite large, making the solid a poor thermal conductor. The present electrical measurement has been taken near room temperature, which was lower than θ_D for device B and much less than θ_D for device A. This result indicated that electrical conduction becomes much less for device A. So, electrical conductivity would increase much for device B. Here, the transport phenomena were supposed to be occurred due to electrons/ polarons hopping with no need for thermal excitations as well as a longer-time regime where thermal excitations[53], which may facilitate the transport process. Estimated relaxation times are found to be low, which may indicate low transit times. Schiff base compounds with metals were extensively investigated by various researchers.[59,61] In particular, one such Schiff base complex[60] has been studied to explore relaxation frequency, relaxation time and dielectric behaviour. It was observed from this study that relaxation frequency increases from 10^2 Hz to 10^3 Hz for the hetero-structure pyridyl Schiff base complex[61] as the external illumination intensity increases from 0 mW cm^{-2} to 24 mW cm^{-2}. But in our cases, relaxation frequency increases from ~ 10^2 Hz to ~ 10^4 Hz for dark to photo conduction for device A and from ~ 10^5 Hz to ~ 10^6 Hz for dark to photo conduction for device B respectively. In the comparative study, it may be concluded that hetero-structure pyridyl Schiff base complex[61] should have lower polarization energy. But the present devices (A and B) should exhibit better

stability due to their wide range of relaxation frequencies as well as multiple transition behavior. Furthermore, the transport phenomena in the present devices (A and B) can be explained by considering the concept of polaron hopping.[59] A polaron was a quasi-particle composed of charge carriers (electron or hole) and its associated self-induced polarization.[59] Holstein and Friedman have developed a small polaron theory and a mechanism of conduction that have been studied by many workers.[56-60] The polaron transport mechanism in the lattice was contingent upon the integral overlap of the electronic wave in adjacent sites.[59] Such a polaron can move less freely than a free electron and as a result, the effective mass of the polaron was larger than the Bloch electron. In the present system, localized states in the mobility gap can be used to trap electrons, which should cause to make distortion for the formation of polarons.

Nowadays, optoelectronic devices based on Si–Ge have been widely used to guide, detect, modulate and generate optical signals.[62] The main challenges using silicon-based detectors lie with the fact that the bandgap of silicon was too large for signal detection at the wavelengths of greatest interest to fibre-optic communication.[62] The use of germanium lowers the bandgap, partly due to strain-induced effects.[61] Despite this, Si–Ge device does not exhibited a lower bandgap. To encounter this issue, zinc complexes, especially **6** has been selected as the alternative materials, which exhibited a much lower bandgap. Additionally, zinc complexes were expected to reduce the absorption coefficient for the generation of less amount of heat in the device/lattice. So, the present zinc complexes, specially complex **6** might turn out to be an important candidate for designing opto-electronic devices of future need.

To correlate the nature of electrical conductivities, we explored different energy components for the stabilization of molecular frameworks for complexes **6** and **5**. The effect of polarisation energy in complex **6** was estimated to be larger, -50.6 kJ/mol compared to the polarisation energy, -24.4 kJ/mol effected in the stabilization of the molecular frameworks of complex **5**. Therefore, on applying a bias voltage, a higher possibility to release the electrons from Zn1–N1 bonding of complex **6** may occur, attributing the higher order of conductivity **(Fig. 6(a))**. Further, the involvement of supramolecular interactions especially C–H···N bonding in the formation of long-range supramolecular crystal architecture of **6** facilitates the conduction mechanism. In complex **6** this interaction was strong enough for long range of frequency and consequently, it did not allow electron/polaron to more hop from one localized state to another.[52] This discussion directly indicates their constant conductivity behavior up to

crossover frequency as evident from **Fig. 6.12(a)**. In the high frequency region, C–H···π interactions are supposed to be much stronger as well as the Zwitterionic nature of the $\mathbf{L^4}$ helps to decrease conductivity value for complex **5**. On the other hand, the C–H···π interactions are expected to be weaker in the case of complex **5** system, which may result in a small range of constant conductivity region up to crossover as mentioned in **Fig. 6.11a**. In addition to this, intermolecular S···H bonding also plays important role in the conduction process. Additional electrons are expected to release from chalcogen (sulphur). As a consequence, conductivity was found to increase after crossover.

To measure the degree of absorption of light by a material at distinct wavelengths, UV-Vis spectroscopy[61] has been used. Here, UV light was made to strike on the matter, the matter absorbs some light and transmission of electrons/ polaron in the matter starts taking place from the state of lower energy to that of higher energy while the rest of the light gets transmitted through it[61]. The absorption occurs when light's energy and the bandgap in the matter were supposed to be the same.[61] To measure the absorption coefficient $\alpha(\nu)$ at distinct wavelengths the following expression can be used[61]: $\alpha(\nu) = \frac{1}{t}\ln\left(\frac{I_i}{I_t}\right)$ where t represents the sample's thickness, I_i denoted incident light intensity, I_t was the transmitted light intensity and the component ln (I_i/I_t) represented the absorbance. The absorbance of the light by a compound in the materials, which mainly occurs because of the chemical structure of the compound or molecule, at various wavelengths was shown by an absorbance spectrum. The absorbance spectrum produced by each compound or molecule was distinct which helps in recognizing the compound. By using the UV-Vis spectra analysis, optical band gap energy E_{opt} of the as-prepared devices (A and B) can be obtained. For calculating E_{opt}, Tauc equation[59] was used which was expressed as $\alpha h\nu = \left[A\left(h\nu - E_{opt}\right)\right]^n$ where α represented absorption coefficient, A was constant and $h\nu$ was photon energy. Exponent n was a constant. Depending on different transition mechanisms, values of n may be 1/2 - for allowed direct, 2 - for allowed indirect, 3/2 – for forbidden direct and 3 - for forbidden indirect). Using Tauc's plot, E_{opt} has been estimated to be 1.77 eV for device A and 2.00 eV for device B (onset band) respectively, which indicate that the present devices were of allowed indirect bandgap semiconductors. [59] In addition, the optical band gaps for other transition bands were also recorded. In this indirect bandgap semiconductor[59], a photon must couple to a phonon to be absorbed. This makes the absorption coefficient

much lower and hence produces less amount of heat in the lattice. So, the stability of the present devices was much higher compared to other semiconductors such as direct bandgap semiconductor.

6.3.8. PXRD analysis

To investigate the crystallinity as well as phase stability of devices A and B before and after the exposure of external light source, the powder XRD (PXRD) studies were carried out in the range of 2θ from 5-80°. The diffraction pattern of various phases gives peaks at 2θ = 7°, 10°, 13°, 15°, 18°, 20°, 22°, 23°, 25°, 27°, 30°, 32°, 33°, 34°, 13°, 42°, 50°, 55°, 65° and 70° from various reflection planes were shown in **Fig. 6.14** and **Fig. 6.15** for devices A and B in their original forms as well as photo-exposed counterpart recovered from the devices.

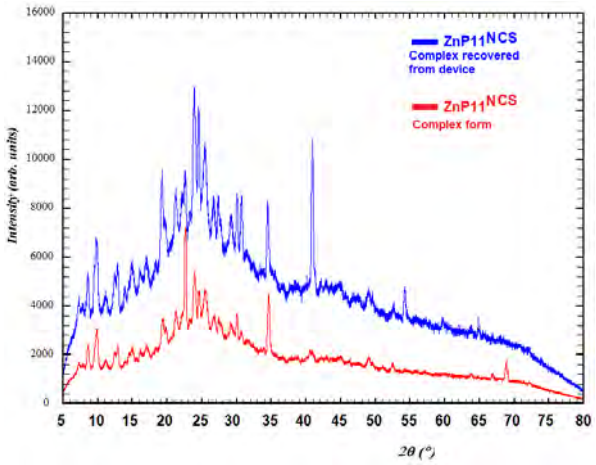

Fig. 6.14. PXRD plots of complex **5** before and after use in device A

In **Fig. 6.14**, the PXRD patterns were compared for the complex **5** compound before and after photo-exposed conditions. Both the compounds show a similar spectral pattern and the peaks match very well, attributing the phase purity of the compounds. In the case of the PXRD spectrum of complex **6** (device B), the patterns for photo-unexposed complex **6** and photo-exposed complex **6** compound recovered from the device B, displayed a similar phase purity. The PXRD analysis of the compounds ensures the phase stability of the compounds (device A and B) in the electrical transport study of the compounds.

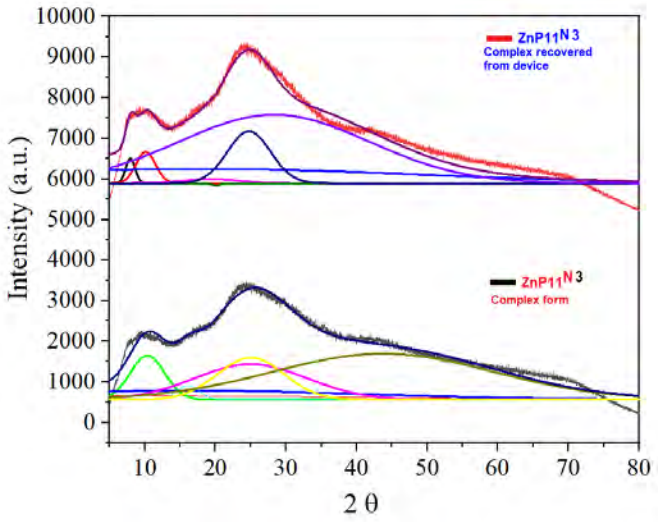

Fig. 6.15. PXRD plots with de-convoluted peaks of complex **6** before and after use in device B construction

We have also made a comparison of DC conductivity for some reported zinc complexes to reveal the efficiency of electrical transport properties. The complex **6** turns out to be a promising candidate among the reported conductivity values (**Table 6.9**).

Table 6.9. Comparison of DC conductivity of the synthetic complexes with the reported zinc complexes

Compounds	DC Conductivity (Ω^{-1} cm^{1}) at dark condition	Ref.
Complex 5	$1.32x10^{-6}$	This Work
Complex 6	0.41	This Work
Zn-(Pymox)Cl_2	9.08×10^{-7}	34
Zn_6(Pymox)$_6$(μ2-O)$_3$	1.25×10^{-6}	34
poly-ZnL^I	0.28	38

6.4. Conclusion

We designed a tetradentate Schiff base following the principle of thermodynamics and synthesised interesting zinc(II) complexes with the ligand and pseudohalides. The zinc complexes exhibited unprecedented ligation motifs as revealed from the crystal structures of the zinc complexes. The mononuclear complex **5** displayed a zwitterionic conformation of the coordinated chelator while the dinuclear complex **6** attributed a tridentate chelating motif in its coordination with Zn(II) ion. The azide and thiocyanate

ions coordinated as homo- and hetero-atomic molecular rods with the terminal binding motif. Both the zinc complexes built beautiful supramolecular frameworks employing extensive H···S/H···N hydrogen bonding and C−H···π interactions. The energy framework analysis of the complexes demarcated the dominant contribution of hydrogen bonding and C−H···π interactions for a structural assortment of the compounds. Further, two electrical devices (A and B) were constructed with the zinc complexes as semiconductors. Room temperature DC conductivity and relaxation time for device A were estimated to be $1.32 \times 10^{-6}\ \Omega^{-1}\ cm^{-1}$ and 0.310 S at the dark condition and $3.20 \times 10^{-6}\ \Omega^{-1}\ cm^{-1}$ and 0.224 S at photo condition, respectively. Similarly, those for device B were estimated to be 0.41 $\Omega^{-1}\ cm^{-1}$ and 0.210 S at the dark condition and 6 $\Omega^{-1}\ cm^{-1}$ and 0.134 S at photo condition, respectively attributing the lower relaxation of complex **6** caused by optical phonon activation. The zinc complexes, specially complex **6** might turn out to be an important candidate for designing opto-electronic devices of future need.

References

[1]. C. N. R. Rao and K. Gopalakrishnan, *ACS Appl. Mater.Interfaces*, 2019, **23**, 19478.

[2]. B. D. Nath, K. Takashi and T. Ema, *Catal. Sci. Technol*., 2020,**10**, 12-34.

[3]. L. L. Feng, G. Yu, Y. Wu, G. D. Li, H. Li, Y. Sun, T. Asefa, W. Chen and X. Zou, *J. Am. Chem. Soc*., 2015, **137**, 14023.

[4]. D. Wu, K. Kusada and H. Kitagawa, *Sci. Technol. Adv.Mater*., 2016, **17**, 583-596.

[5]. H. L. C. Feltham and S. Brooker, *Coord. Chem. Rev*., 2014, **276**, 1−33.

[6]. M. N. Leuenberger and D. Loss, *Nature*., 2001, **410**, 789−793.

[7]. F. Troiani and M. Affronte, *Chem. Soc. Rev*., 2011, **40**, 3119−3129.

[8]. K. V. Raman, A. M. Kamerbeek, A. Mukherjee, N. Atodiresei, T. K. Sen, P. Lazić, V. Caciuc, R. C. Michel, D. Stalke, S. K. Mandal, S. Blügel, M. Münzenberg and J. Moodera, *Nature*, 2013, **493**, 509-513.

[9]. T. Kimura, *Annu. Rev. Mater. Res*., 2007, **37**, 387-413.

[10]. J. D. Blakemore, N. D. Schley, D. Balcells, J. F. Hull, G. W. Olack, C. D. Incarvito, O. Eisenstein, G. W. Brudvig and R. H. Crabtree, *J. Am. Chem. Soc*., 2010, **132**, 16017.

[11]. M. Yoshida, S. Masaoka, J. Abe and K. Sakai, *Asian J. Chem*., 2010, **5**, 2369.

[12]. D. J. Wasylenko, C. Ganesamoorthy, M. A. Henderson and C. P. Berlinguette, *Inorg. Chem*., 2011, **50**, 3662.

[13]. S. K. Mandal and H. W. Roesky, *Acc. Chem. Res*., 2010, **43**, 248-259.

[14]. A. E. Thuijs, X. –G. Li, Y. –P. Wang, K. A. Abboud, X. -G. Zhang, H. –P. Cheng and G. Christou, *Nat. Commun*., 2017, **8**, 500.

[15]. R. Majee, A. Kumar, T. Das, S. Chakraborty and S. Bhattacharyya, *Angew. Chem.*, 2020, **59**, 2881-2889.

[16]. M. Mauro, K. C. Schuermann, R. Prétôt, A. Hafner, P. Mercandelli, A. Sironi and L. De Cola, *Angew. Chem.*, 2010, **49**, 1222 –1226.

[17]. R. Xiong, D. Mara, J. Liu, R. Van Deun and K. E. Borbas, *J. Am. Chem. Soc*. 2018, **140**, 10975–10979.

[18]. S. V. Eliseeva and J. -C. G. Bünzli, *Chem. Soc. Rev*., 2010, **39**, 189-227.

[19]. J. -C. G. Bünzli and S. V. Eliseeva, *J. Rare Earths*., 2010, **28**, 824-842.

[20]. M. Karar, P. Paul, B. Biswas, T. Majumdar and A. Mallick, *J. Chem. Phys*. 2020, **152**, 075102.

[21]. P. K. Mudi, A. Das, N. Mahata and B. Biswas, *J. Mol. Liq*., 2021, **340**, 117193.

[22]. S. Roy, P. Paul, M. Karar, M. Joshi, S. Paul, A. R. Choudhury and B. Biswas, *J. Mol. Liq*. 2021, **326**, 115293.

[23]. A. Mallick, *Chem. Commun*., 2014, **50**, 6890-6893.

[24]. N. Chattopadhyay, *J. Lumin.,* 2006, **118**, 165-172.

[25]. P. Paul, A. Mallick and T. Majumdar, *ACS Appl. Electron. Mater*., 2021, **3 (8)**, 3588-3598.

[26]. P. Hanggi, M. Ratner and S. Yaliraki, *Chem. Phys*., 2002, **281**, 111.

[27]. J. R. Reimers, *Ann. N.Y. Acad. Sci*., 2003, **1006**, 1-332.

[28]. C. K. Pal, S. Mahato, H. R. Yadav, M. Shit, A. R. Choudhury and B. Biswas, *Polyhedron*, 2019, **174**, 114156.

[29]. D. Dey, M. Patra, A. Al-Hunaiti, H. Yadav, A. Al-mherat, S. Arar, M. Maji, A. R. Choudhury and B. Biswas, *J. Mol. Struct*., 2019, **1180**, 220-226.

[30]. D. Dey, A. De, H. R. Yadav, P. S. Guin, A. R. Choudhury, N. Kole and B. Biswas, *ChemistrySelect*, 2016, **1**, 1910-1916.

[31]. S. Bhunia, S. Chandel, S. K. Karan, S. Dey, A. Tiwari, S. Das, N. Kumar, R. Chowdhury, S. Mondal, I. Ghosh, A. Mondal, B. B. Katua, N. Ghosh and C. M. Reddy, *Science*, 2021, **373**, 321-327.

[32]. S. Das, A. Mondal and C. M. Reddy, *Chem. Soc. Rev*, 2020, **49**, 8873-8877.

[33]. M.M. Shehata, M. S. Adam, K. Abdelhady and M. M. Makhlouf, *J. Solid State Electrochem*., 2019, **23(8)**, 2519-2531.

[34]. S. Konar, A. Dey, S. R. Choudhury, K. Das, S. Chatterjee, P. P. Ray, J. Ortega-Castro, A. Frontera and S. Mukhopadhyay, *J. Phys. Chem. C*., 2018, **122(16)**, 8724-8734.

[35]. S. Wang, B. Zhang, Y. Hou, C. Du and Y. Wu, J. Mater. Chem. C., 2013, **1(3)**, 406-409.

[36]. L. Chen, J. Qiao, J. Xie, L. Duan, D. Zhang, L. Wang and Y. Qiu, *Inorg. Chim. Acta*., 2009, **362(7)**, 2327-2333.

[37]. A. Irfan, A. G. Al-Sehemi, M. A. Assiri and S. Ullah, *Mater. Sci. Semicond.Process*., 2020, **107**, 104855.

[38]. M. T. Nguyen, R. A. Jones and B. J. Holliday, Macromolecules, 2017, **50(3)**, 872-83.

[39]. R. Chouk, C. Aguir, M. Bergaoui, J. P. Djukic, C. Bouzidi and M. Khalfaoui, *Opt. Quantum Electron*., 2021, **53(4)**, 1-20.

[40]. P. K. Mudi, N. Bandopadhyay, M. Joshi, M. Shit, S. Paul, A. R. Choudhury and B. Biswas, *Inorg. Chim. Acta*., 2020, **505**, 119468.

[41]. P. K. Mudi, S. Pradhan, A. Sahu, D. Saha and B. Biswas, *Journal of Applied Microbiology: Theory & Technology*, 2021, **2**, 18-28.

[42]. CrysAlisPro 1.171.39.35c, 2017, Rigaku Oxford Diffraction, Rigaku Corporation: Tokyo, Japan.

[43]. G. M. Sheldrick, Acta Crystallogr., Sect. A: Found. Adv., 2015, **71**, 3–8.

[44]. G. M. Sheldrick, Acta Crystallogr., Sect. C: Struct. Chem., 2015, **71**, 3–8.

[45]. O. V. Dolomanov, L. J. Bourhis, R. J. Gildea, J. A. K. Howard and H. Puschmann, J. *Appl. Crystallogr*., 2009, **42**, 339–341.

[46]. M. J. Turner, J. J. McKinnon, S. K. Wolff, D. J. Grimwood, P. R. Spackman, D. Jayatilaka and M. A. Spackman, Crystal Explorer, University of Western Australia, http://hirshfeldsurface.net17, 2017.

[47]. M. A. Spackman and D. Jayatilaka, *Cryst. Eng. Comm*., 2009, **11**,19-32.

[48]. M. A. Spackman and J. J. McKinnon, *Cryst. Eng. Comm*., 2002, **4**, 378-392.

[49]. T. Roisnel and J. Rodriguez-Carvajal, *WinPLOTR: A windows tool for powder diffraction pattern analysis*. *Mater. Sci. Forum*, Barcelone. 2001, 268-273.

[50]. S. Mahato, N. Meheta, K. Muddukrishnaiah, M. Joshi, M. Shit, A. R. Choudhury and B. Biswas, *Polyhedron*, 2021, **194**, 114933.

[51]. A. De, D. Dey, H. R. Yadav, M. Maji, V. Rane, R. M. kadam, A. R. Choudhury and B. Biswas, *J. Chem. Sci*., 2016, **128**, 1775-1782.

[52]. B. Biswas, M. Patra, S. Dutta, M. Ganguly and N. Kole, *J. Chem. Sci.*, 2013, **125**, 1445-1453.

[53]. C. K. Pal, S. Mahato, M. Joshi, S. Paul, A. R. Choudhury and B. Biswas, *Inorg. Chim. Acta*, 2020, **506**, 119541.

[54]. P. K. Mudi, R. K. Mahato, M. Joshi, S. Paul, A. R. Choudhury and B. Biswas, *J. Mol. Struct*., 2020, **1200**, 127083.

[55]. P. K. Mudi, R. K. Mahato, M. Joshi, M. Shit, A. R. Choudhury, H. S. Das, and B. Biswas, *Appl. Organomet. Chem*., 2021, **35**, e6211.

[56]. P. Pal and A. Ghosh, *J. Appl. Phys*., 2021, **129,** 234102.

[57]. U. Hoppe, A. Ghosh, S. Feller, A. C. Hannon and J. Neuefeind, *J. Non-Cryst. Solids*, 2021, **572**, 121120.

[58]. S. Das and A. Ghosh, *J. Non-Cryst. Solids*, 2017, **28**, 458.

[59]. S. Bhattacharya, Metal Oxide Glass Nanocomposites, Elsevier Publications, 2020, 27-35.

[60]. S. Kabi and A. Ghosh, *Mater. Res. Bull*., 2013, **48**, 3405.

[61]. M. Silver and H. Bassle, *Philosophical Magazine Letters,* 1987, **56**, 109-112.

[62]. J. Liu, R. Camacho-Aguilera, J. T. Bessette, X. Sun, X. Wang, Y. Cai, L. C. Kimerling and J. Michel, Thin Solid Films, 2012, **520**, 3354.